REPORT DOCUMENTATION PAGE

1. REPORT DATE (DD-MM-YYYY)	2. REPORT TYPE	3. DATES COVERED (From - To)
21-01-2012	Final	15-05-2008 -- 30-09-2011

4. TITLE AND SUBTITLE
A Multi-Scale Structural Health Monitoring Approach for Damage Detection, Diagnosis and Prognosis in Aerospace Structures

Note: Official title is "Ultrasonic Structural Health Monitoring under Complex Conditions"

5a. CONTRACT NUMBER

5b. GRANT NUMBER
FA9550-08-1-0241

5c. PROGRAM ELEMENT NUMBER

6. AUTHOR(S)
Michaels, Jennifer E.
Jacobs, Laurence J.
Ruzzene, Massimo

5d. PROJECT NUMBER

5e. TASK NUMBER

5f. WORK UNIT NUMBER

7. PERFORMING ORGANIZATION NAME(S) AND ADDRESS(ES)
Georgia Tech Research Corporation
Georgia Institute of Technology
Atlanta, GA 30332-0420

8. PERFORMING ORGANIZATION REPORT NUMBER

9. SPONSORING/MONITORING AGENCY NAME(S) AND ADDRESS(ES)
Air Force Office of Scientific Research
875 North Randolph Street, Suite 326
Arlington, VA 22203-1768

10. SPONSOR/MONITOR'S ACRONYM(S)
AFOSR

11. SPONSOR/MONITOR'S REPORT NUMBER(S)
AFRL-OSR-VA-TR-2012-0260

12. DISTRIBUTION/AVAILABILITY STATEMENT
Unlimited distribution.

13. SUPPLEMENTARY NOTES

14. ABSTRACT
This project has developed multi-scale methods for structural health monitoring to better understand, analyze and quantify the progression of damage at multiple length scales. Benchmark experiments were performed to relate nonlinearity measured with ultrasonic Lamb waves to plastic strain and fatigue life. Theory was developed and validated to predict second harmonic generation for specific mode/frequency pairs. A suite of advanced imaging methods was developed and demonstrated for detecting, locating and characterizing damage using both spatially distributed arrays and guided wavefield measurements. A model-based parameter estimation method was developed and validated to estimate dispersion curves, propagation loss, transducer distances and transducer transfer functions using minimal a priori information. The multi-scale finite element method was developed to bridge a fine-scale mesh around a defect and a coarse-scale discretization of the entire domain. It was validated by comparing scattering of guided waves from damage in a plate with analytical and numerical solutions, and was shown to produce very high quality results using an order of magnitude less computational resources compared to traditional methods.

15. SUBJECT TERMS
Structural Health Monitoring, Nonlinear Ultrasonics, Guided Waves, Spatially Distributed Arrays, Adaptive Imaging, Dispersion Estimation, Wave Propagation Modeling, Multi-Scale Finite Element Method

16. SECURITY CLASSIFICATION OF:			17. LIMITATION OF ABSTRACT	18. NUMBER OF PAGES	19a. NAME OF RESPONSIBLE PERSON
a. REPORT	b. ABSTRACT	c. THIS PAGE			Jennifer E. Michaels
UU	UU	UU	UU	29	19b. TELEPHONE NUMBER (Include area code) 404-894-2994

A Multi-Scale Structural Health Monitoring Approach for Damage Detection, Diagnosis and Prognosis in Aerospace Structures

Jennifer E. Michaels (PI)[1], Laurence J. Jacobs[2,3], and Massimo Ruzzene[3,4]

[1]School of Electrical and Computer Engineering
[2]School of Civil and Environmental Engineering
[3]The George W. Woodruff School of Mechanical Engineering
[4]The Daniel Guggenheim School of Aerospace Engineering
Georgia Institute of Technology

January 20, 2012

1. Introduction

This project has developed multi-scale methods for structural health monitoring (SHM) to better understand, analyze and quantify the progression of damage starting from the characterization of its precursors, moving ahead to estimating its location, type and extent, and finally investigating its effects at the component and structural levels. Fatigue and damage generation and progression are processes consisting of a series of interrelated events that span large scales of space and time. These spatial and temporal scales have to be considered at a fundamental level to effectively integrate damage detection and characterization with damage prediction and life estimation. Hence, the analysis of damage evolution needs to be accompanied by appropriate interrogation methods capable of monitoring damage progression over these scales. This project has considered dynamics-based monitoring with elastic waves and mechanical vibrations for which the spatial and temporal scales can be related to the frequency and time span of interrogation as illustrated in Figure 1. When the component is excited at frequencies close to its main natural modes of vibration, it will undergo a response which can be considered as "global." As the frequency of inspection is increased, the response becomes more localized around the excitation region, and the recorded behavior becomes more sensitive to small local variations. Such local variations include macroscopic single cracks or clusters, which can typically be detected by low-to-medium frequency guided and bulk ultrasonic waves, and microscopic cracks, material nonlinearities or dislocations pile-ups as detected by nonlinear ultrasonic methods. Such a unified approach to structural health monitoring can therefore be envisioned where the spatial resolution and types of damage that can be detected span a continuum from the local and microscopic to the global and macroscopic. Reported here are a suite of such methods, along with the corresponding fundamental theory, that are anticipated to become the foundation of practical SHM methods for the Air Force, providing a better diagnosis and prognosis than would be possible with a single interrogation method alone.

This final report covers the time period of May 15, 2008 through September 30, 2011, for AFOSR Grant Number FA9550-08-1-0241. The project accomplishments fall into three general categories: (1) Nonlinear ultrasonics, (2) spatially distributed ultrasonic arrays, and (3) structural effects of damage. A summary of results is reported in Sections 2, 3 and 4, and a comprehensive list of publications resulting from this project is provided in Section 5 (References). Appropriate reviews of the literature can be found in the individual publications and are not repeated in this document.
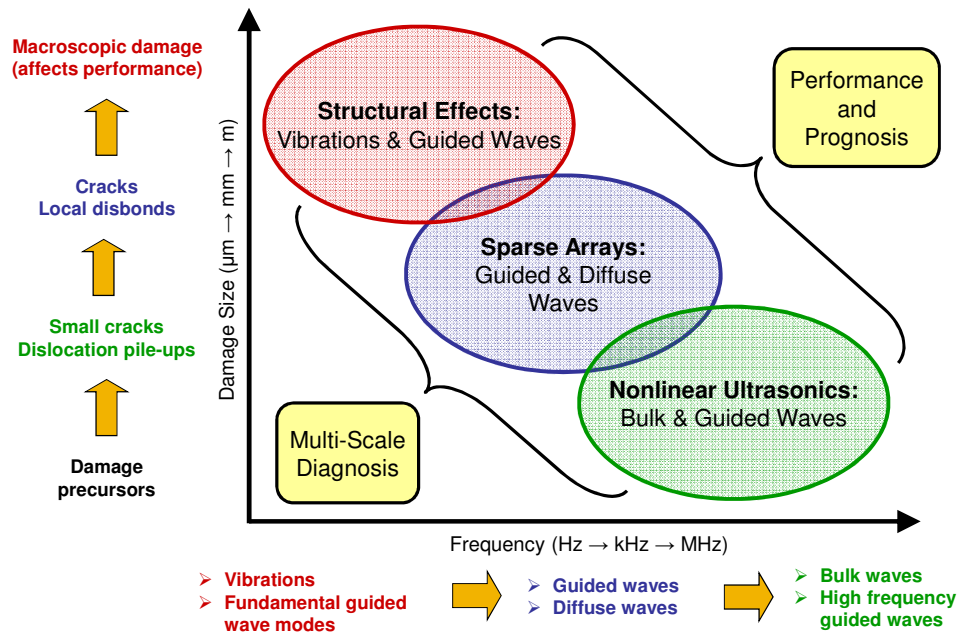
FIGURE 1. Overview of multi-scale structural health monitoring.

2. Nonlinear Ultrasonics

2.1 Relationship between acoustic nonlinearity measured with multi-mode, dispersive Lamb waves, measured plastic strain and fatigue life

A set of experiments were completed that worked to relate the acoustic nonlinearity measured with Lamb waves to both the measured plastic stain and the remaining fatigue life. This set of benchmark measurements is being used to develop the physical mechanism behind the generation of acoustic nonlinearity in metals. Consider a set of three fatigue specimens made of 1.6 mm thick Al-1100-H14 plate. These specimens were loaded in low cycle fatigue, and the resulting measured plastic strain versus fatigue cycles are shown in Figure 1.

FIGURE 1. Measured cumulative plastic strain versus fatigue cycle number.

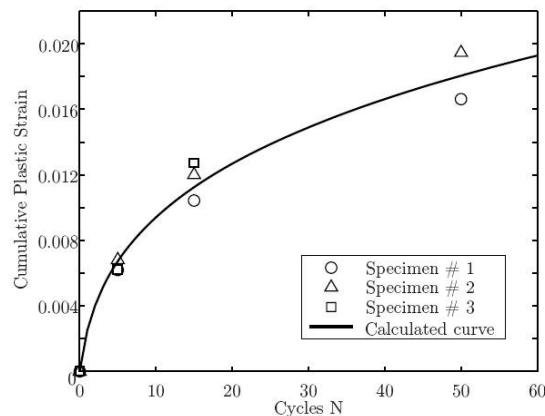Next consider the normalized acoustic nonlinearity measured with multi-mode, dispersive Lamb waves.   Figures 2(a) and (b) shows this measured acoustic nonlinearity as a function of percentage of fatigue life, including the error bars. Finally Figure 2(c) shows the relationship between the acoustic nonlinearity and measured plastic strain. Additional details regarding this work can be found in [1-3].

(a)

(b)

(c)
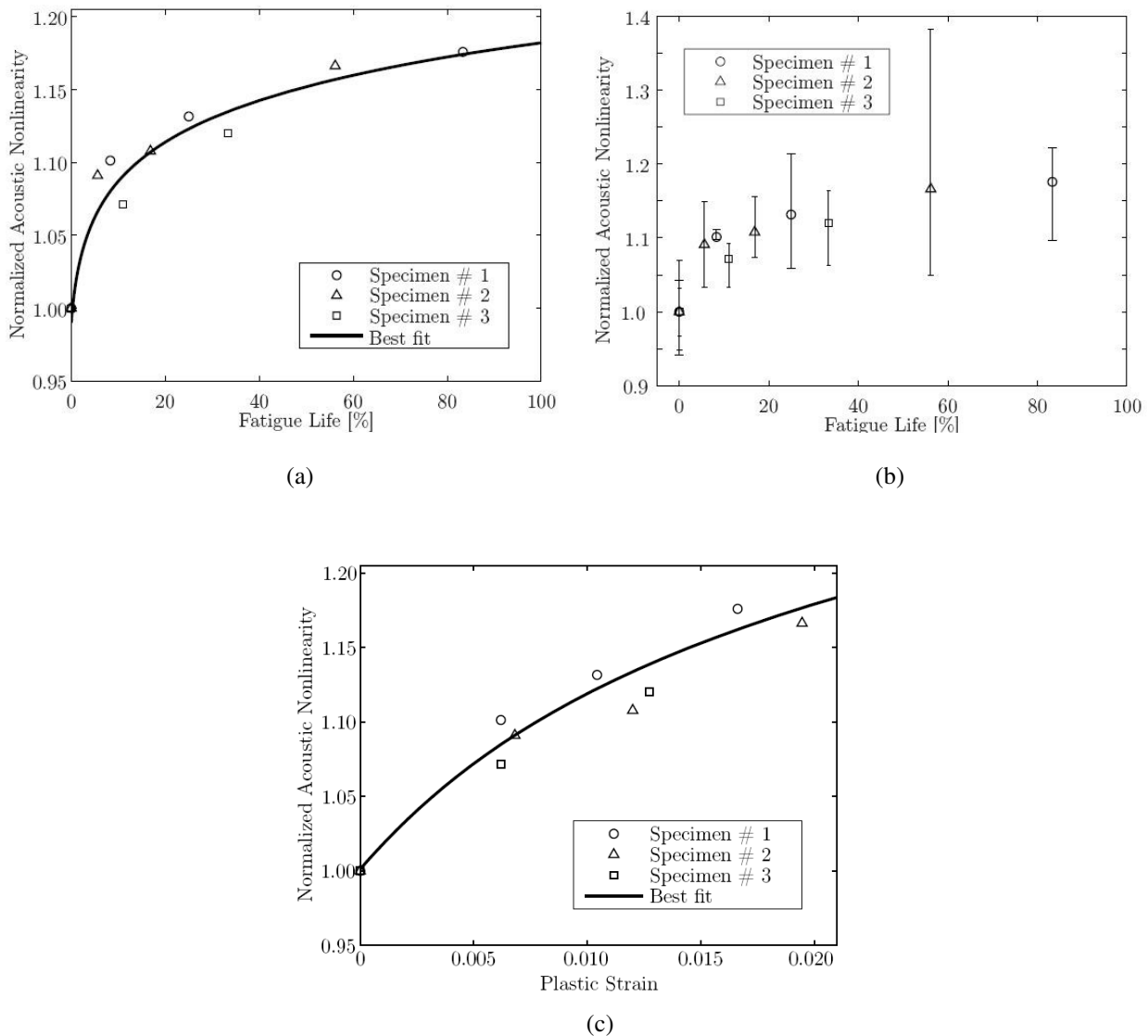
FIGURE 2. (a) Mean values and best fit of normalized acoustic nonlinearity versus percent of fatigue life (b) error bars, and (c) normalized acoustic nonlinearity versus plastic strain.

2.2   Influence of residual stress on acoustic nonlinearity measured with Rayleigh surface waves

This portion of the research has examined the influence of surface conditions, such as residual stress, on the measured acoustic nonlinearity. A series of 7075 aluminum specimens were subjected to different levels of shot peening to induce near surface residual stresses. One

specimen was kept un-peened as a reference, the second one was shot peened with the Almen intensity of 8A, and the other with the intensity of 16A. The shot peening was performed with 0.023 in. diameter cast steel shot and 100% coverage. The original specimen was ground by low-stress hand polishing with polishing paper and lubrication oil, while the other two remained unpolished. Figure 4 shows the measured acoustic nonlinearity for each of these three specimens as a function of propagation distance. Note that acoustic nonlinearity should be cumulative (linearly proportional) to propagation distance and the slope of these lines are indicators of the degree of material nonlinearity. Figure 4 clearly shows the increase in measured acoustic nonlinearity as a function of residual stress. It also shows that the surface roughness of the shot peened samples causes the measured second harmonic to saturate quickly and thus attenuate sharply with the propagation distance. Refer to [7] and [8] for additional details.
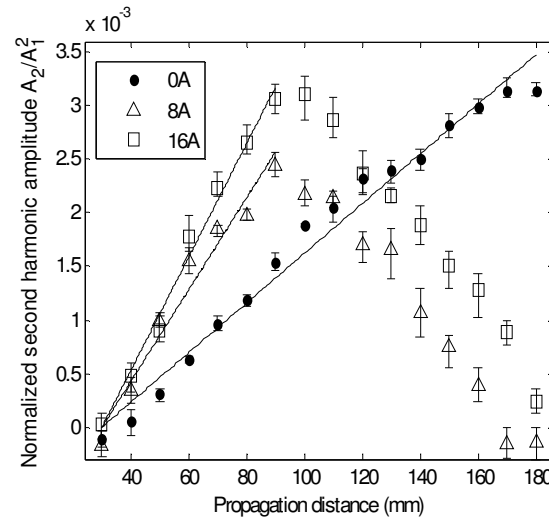

FIGURE 4. Variation of the normalized second harmonic amplitude as a function of propagation distance for original sample (0A), shot peened with intensity of 8A, and shot peened with intensity of 16A.

2.3   Numerical modeling to quantify boundary effects in nonlinear ultrasonic wave propagation

Numerical simulations were performed to quantify the influence of boundary conditions on propagating nonlinear ultrasonic waves. This work is essential to understand the propagation of nonlinear ultrasonic waves in complex components. This study considers the propagation of nonlinear waves in an elastic half-space with quadratic nonlinearity subjected to different types of boundary conditions. These boundary conditions are either prescribed displacements or tractions. It is found that in addition to the generation of higher harmonics (second order and above), a traction boundary condition will also generate a static (zero frequency) nonlinear term. This is in contrast to a displacement boundary condition that only generates higher harmonics. This zero frequency term is independent of propagation distance, and has the potential to be used to as an additional measure of material nonlinearity induced by fatigue damage. Additional work focused on the analytical solution for the propagation of an acoustic pulse in an elastic medium with weak quadratic nonlinearity. Here, both a displacement pulse and a stress pulse of arbitrary shapes were used to generate the wave motion in the solid. By obtaining the explicit solutions for arbitrary pulse shapes, it was shown that for a sinusoidal tone-burst, in addition to a second order harmonic field, a radiation induced static strain field is also generated. These results help clarify

some confusion in the recent literature regarding the shape of the propagating static displacement pulse. Work published in [4,5,6] and [12,13] provides additional information.

2.4   Efficiency for experimentally generating nonlinear Lamb waves

Consider wave propagation in an isotropic, homogeneous, nonlinear elastic infinite plate. It has been shown that only specific Lamb wave modes generate a second harmonic component, and criteria include phase and group velocity matching of the primary and secondary wave modes, and non-zero power flux from the primary and secondary wave modes [9,10]. The primary Lamb wave mode and its corresponding secondary mode are termed a *mode pair*, and examples of pairs that satisfy the above criteria are plotted on the phase velocity plot given in Figure 5.
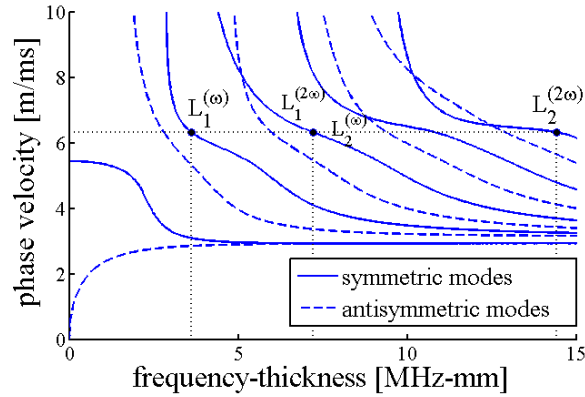

FIGURE 5. Phase velocity plot of symmetric and antisymmetric Lamb wave modes, indicating mode pairs that exhibit second harmonic generation (note that the superscript designates a wave mode as primary vs. secondary).

It has been shown that the amplitudes, which are proportional to the displacement, of the primary and secondary wave modes that satisfy these criteria follow the trend

$$\frac{A_2}{A_1^2} \propto z \kappa_L^2 \beta \tag{1}$$

where A_1 is the amplitude of the primary wave, A_2 is the amplitude of the secondary wave, z is the propagation distance along the propagation direction, $\kappa_L = \omega/c_{ph}$ is the wavenumber of the primary Lamb wave with frequency ω and phase velocity c_{ph}, and β is the acoustic nonlinearity parameter. It has been shown that β relates to an intrinsic material parameter that evolves with increasing material damage. Results shown here for acoustic nonlinearity measured with Lamb wave mode pairs are based on previous experimental results for the mode pairs s1-s2 and s2-s4.

In contrast to Lamb waves, Rayleigh waves propagate when the thickness is very large compared to the wavelength and thus propagate along the surface of the material with wave energy concentrated mostly within a depth of about one wavelength. Since these waves are non-dispersive, theoretically any ultrasonic frequency wave could generate a second harmonic wave. Previous research has shown the relation between amplitudes of primary and secondary Rayleigh waves to be of a similar form as for Lamb waves. For both guided waves there is a linear relationship between the amplitude ratio A_2/A_1^2 and propagation distance z, so by measuring both primary and secondary wave amplitudes at different propagation distances a relative value for parameter β can be experimentally determined.

Experiments were performed to excite Lamb waves in an aluminum 6061-T6 plate of thickness 1.6 mm by the wedge generation method, and Rayleigh waves were similarly generated in a thicker plate (3.175 mm). A schematic of the experimental setup is shown in Figure 6. Note that different wedge fixtures are needed for the Rayleigh and Lamb waves since their phase velocities are different, and thus there is a different amount of wave propagation (and associated attenuation) through the wedge material for each wave. A 35-cycle sinusoidal input signal at the chosen excitation for the specific guided wave is generated by a high-power-gated amplifier and transferred to a narrowband commercial piezoelectric transducer with a radius of 6.25 mm and center frequency of either 2.25 MHz or 5 MHz. A transducer with center frequency of twice the excitation frequency simultaneously detects the primary and secondary wave in the far field of the transmitting transducer, at propagation distances ranging from 20-50 cm for the Lamb waves, and 5-20 cm for the Rayleigh waves. All experimental parameters are summarized in Table 1. The time-domain signal is then transferred to an oscilloscope, averaged extensively to improve the signal-to-noise ratio, and then transferred to a PC for post digital processing.   Each measurement was taken three times and averaged for error analysis.
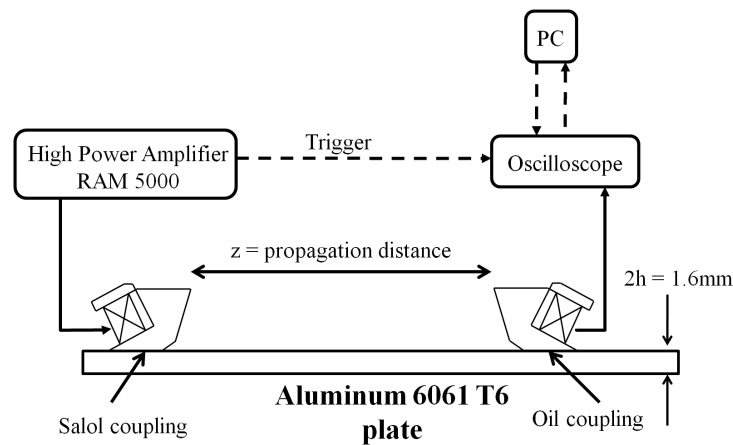

FIGURE 6. Schematic of experimental setup for Rayleigh and Lamb wave measurements of second harmonic generation.

TABLE 1. Rayleigh and Lamb wave experimental parameters.

Guided wave	Excitation frequency	Wave phase velocity	Sample thickness	z (cm)	z_w (cm)	Coupling
Lamb wave s2-s4 (L_2)	4.5 MHz	6320 m/s	1.6 mm	20-50	0.6	salol/oil
Lamb wave s1-s2 (L_1)	2.25 MHz	6320 m/s	1.6 mm	20-50	0.6	salol/oil
Rayleigh wave	5 MHz	2920 m/s	3.175 mm	6-18	1.2	oil/oil
Rayleigh wave	4.5 MHz	2920 m/s	3.175 mm	6-20	1.2	oil/oil

Lamb wave signals are analyzed in the frequency domain via the short-time Fourier transform to extract the primary and secondary wave amplitudes. Rayleigh waves are neither dispersive nor multimodal, so the signal processing technique is somewhat simplified. The steady-state portion of the Rayleigh wave signal is isolated, a Hann window is applied, and a fast Fourier transform

(FFT) is applied to the resulting processed signal. The primary and secondary amplitudes are extracted from the frequency spectrum. Representative time signals and spectral analyses for both Rayleigh and Lamb waves are shown in Figure 7 and Figure 8, respectively.
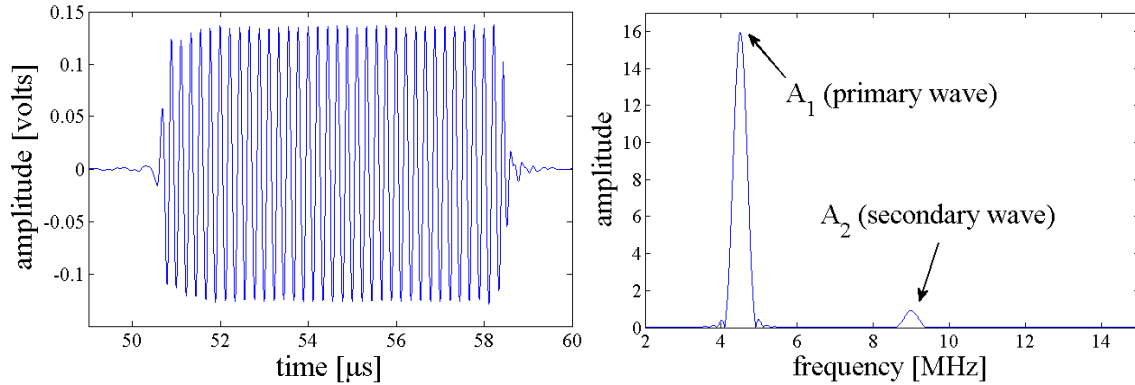

FIGURE 7. Representative time signal (left) and frequency spectrum (right) for a primary and secondary Rayleigh wave at a propagation distance of 8cm.
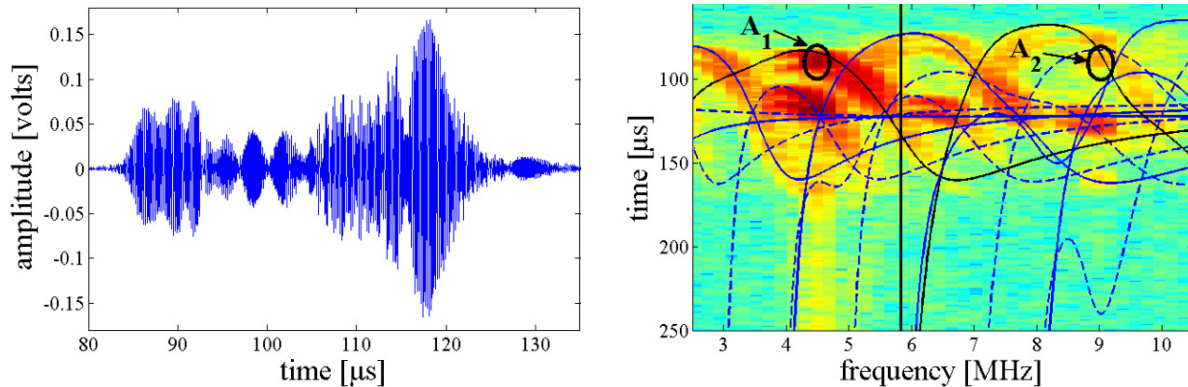

FIGURE 8. Representative time signal (left) and time-frequency spectrogram (right) for Lamb wave received at a propagation distance of 32.5 cm.

The finite aperture and bandwidth of the transducer-wedge detection method presents some obstacles in comparing signals from modes at different frequencies and phase velocities. Appropriate amplitude corrections can be used to obtain meaningful data to compare the second harmonic generation detected by the different modes. First, the primary wave propagating through the aluminum plate will diffract due to beam spreading, thus decreasing the amplitude of the measured primary wave. When the primary and secondary waves propagate through the wedge on the receiving side, the wedge material (acrylic) attenuates the wave amplitude, and this attenuation is frequency dependent. Due to the bandwidth of the receiving transducer, the transducer will detect different frequencies with varying efficiency, and this transducer efficiency can be characterized and accounted for by its frequency response function. Furthermore, in order to isolate the material nonlinearity in the experimental results, the instrumentation nonlinearity of the transducers and amplification system must be subtracted out from the signal results, particularly since different transducer pairs are used to excite and

measure the different wave modes. These various corrections, which are described in detail in [11], enable nonlinear parameters measured with different transducer pairs to be quantitatively compared.

The results for measurement of the acoustic nonlinearity using both Lamb and Rayleigh waves are shown in Figure 9 and summarized in Table 2. The error bars represent the standard deviation of the data points based on three independent measurements. Graphical results are normalized in terms of the largest plotted value. Tabulated results for the nonlinear parameter are normalized in terms of the value measured from the s1-s2 Lamb wave mode.
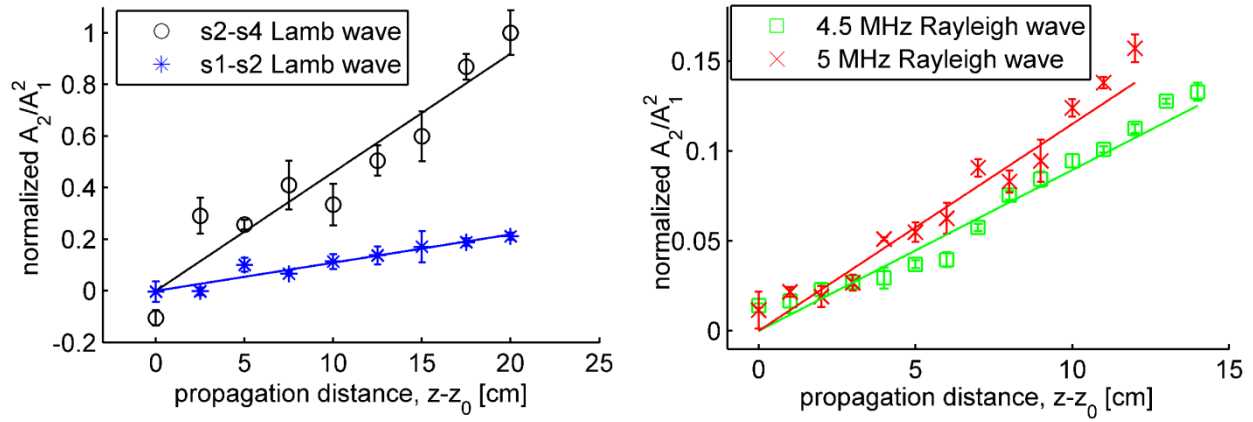
FIGURE 9.   Measurement results for normalized acoustic nonlinearity parameter over normalized propagation distance for Lamb wave modes s2-s4 and s1-s2 (left) and Rayleigh waves at 4.5 MHz and 5 MHz (right).

TABLE 2. Summary of results for measurement of acoustic nonlinearity using Rayleigh and Lamb wave modes.

Guided wave mode	$\dfrac{\beta'}{\beta'_{s1-s2}}$	Distance of linear trend	Maximum measurement error	Coefficient of determination, R^2
Lamb wave s2-s4 (L_2)	4.23	20 cm	8.3%	0.9026
Lamb wave s1-s2 (L_1)	1	20 cm	12.9%	0.9310
Rayleigh wave 5 MHz	0.787	13 cm	23.1%	0.9378
Rayleigh wave 4.5 MHz	0.15	15 cm	8.7%	0.9319

It was found that the s2-s4 Lamb wave mode exhibited the largest acoustic nonlinearity, and the 4.5 MHz Rayleigh wave the smallest. The difference in measured values of acoustic nonlinearity from the s2-s4 mode and s1-s2 mode is due to excitation frequency. The Lamb waves had a

larger range of ability to measure the acoustic nonlinearity parameter compared to the Rayleigh waves. It was found that out of the four considered guided waves, the s2-s4 Lamb wave was the least accurate in measuring the expected linear trend of acoustic nonlinearity over propagation distance. Since the Lamb waves measured the highest amount of acoustic nonlinearity over the largest distance, they are potentially more sensitive to the acoustic nonlinear parameter. However, due to its low measurement error and high accuracy in measuring the linear trend of acoustic nonlinearity, the 4.5 MHz Rayleigh wave would be preferred over other wave modes.

This research has investigated the feasibility of measuring acoustic nonlinearity in undamaged aluminum 6061 with different ultrasonic guided wave modes. The acoustic nonlinearity parameter measures the second harmonic component generated as a pure sinusoidal ultrasonic wave propagates through the aluminum material.   This parameter has the potential to characterize material damage prior to crack initiation since previous work has shown a relation between this parameter and increasing fatigue damage, thus it could provide important health monitoring information of structural materials for more accurate life prediction models. Additional details are found in [9-11].

3   Spatially Distributed Ultrasonic Arrays

Spatially distributed arrays consist of individual piezoelectric transducers that are sparsely distributed over a region of interest. The transducers, which are Lead Zirconate Titanate (PZT) discs, are permanently attached to the structure, and each one can act as either transmitter or receiver of guided elastic waves. The focus of the research activities in this general area has been to develop algorithms to enable quantitative assessment of structural damage based upon recorded guided wave signals.   Key results are reported as per the following categories: (1) Imaging algorithms, (2) damage characterization, (3) model-based parameter estimation, (4) environmental effects, and (5) supporting efforts.

3.1   Guided wave imaging algorithms

Several imaging algorithms have been implemented for localizing damage in plate-like structures. Delay-and-sum (DAS) type algorithms can be effective for damage localization, but there are typically significant imaging artifacts. The MVDR (minimum variance distortionless response) adaptive algorithm, which is essentially delay-and-sum imaging with adaptive weights, provides significant reduction of artifacts but requires knowledge of scattering characteristics. Both of these algorithms are applied to the differenced, or residual, signals of a sparse array where baseline signals are subtracted from current signals. In essence, the signal changes are imaged. This subtraction is advantageous for a sparse array because, unlike a compact linear or circular array that relies upon backscattered waves, damage can be introduced in between array elements, and forward scattered signals cannot be readily separated from the direct arrivals. Both DAS and MVDR imaging can be performed on either envelope-detected signals or raw (RF) waveforms. Figure 10 shows imaging results for a 6 mm drilled through-hole in an aluminum plate, and illustrates the improvement obtained when using MVDR compared to DAS. There is an improvement of about 10 dB going from DAS to MVDR using envelope-detected signals, and there is a significant improvement in resolution when using phase information (i.e., imaging with the RF signals).
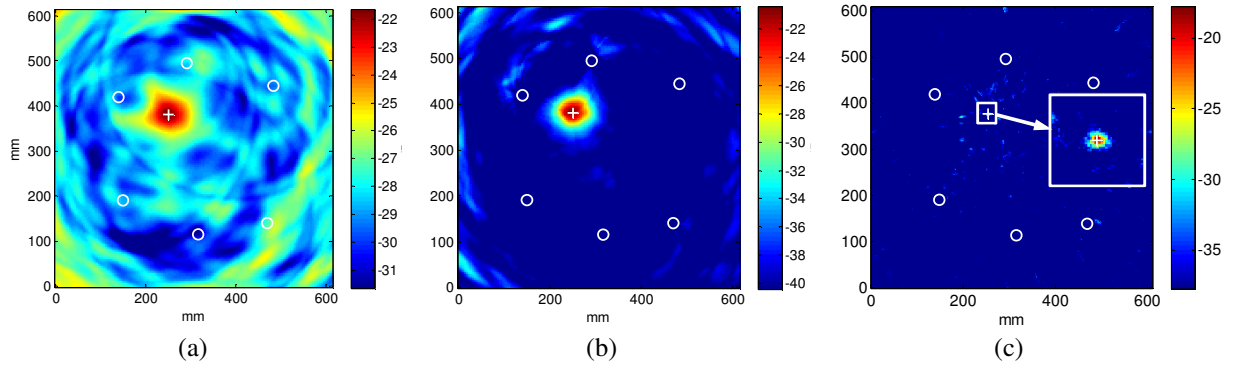
FIGURE 10. Images from experimental data for a 6 mm diameter through hole. (a) Delay-and-sum imaging with envelope data (10 dB color scale), (b) MVDR imaging with envelope data (20 dB color scale), and (c) MVDR imaging with RF data (20 dB color scale, note zoomed image around scatterer). The open circles are the transducer locations, and the "+" is the location of the scatterer.

The significance of MVDR imaging is that it provides considerably improved results as compared to DAS imaging but with only a modest increase in the computational burden. For some cases, it is also less sensitive to signal-baseline mismatch caused by changes in operational or environmental conditions. Additional information can be found in references [14,22-24].

A new imaging algorithm, referred to here as Sparse Reconstruction (SR), was developed to utilize the *a priori* information that damage is sparse. The DAS and MVDR algorithms are not able to take this information into account, which leads to imaging artifacts. The idea of the SR method is to select pixel values that provide a balance between explaining the data and being spatially sparse. This is accomplished here by using basis pursuit denoising combined with a reasonable model of the guided wave propagation and scattering in the plate. Experimental results are shown in Figure 11 for one and two glued-on masses, which act as scatterers of guided waves and thus simulate damage. What is noteworthy is the complete lack of imaging artifacts away from the actual scattering sites, which is a direct result of the sparsity assumption.
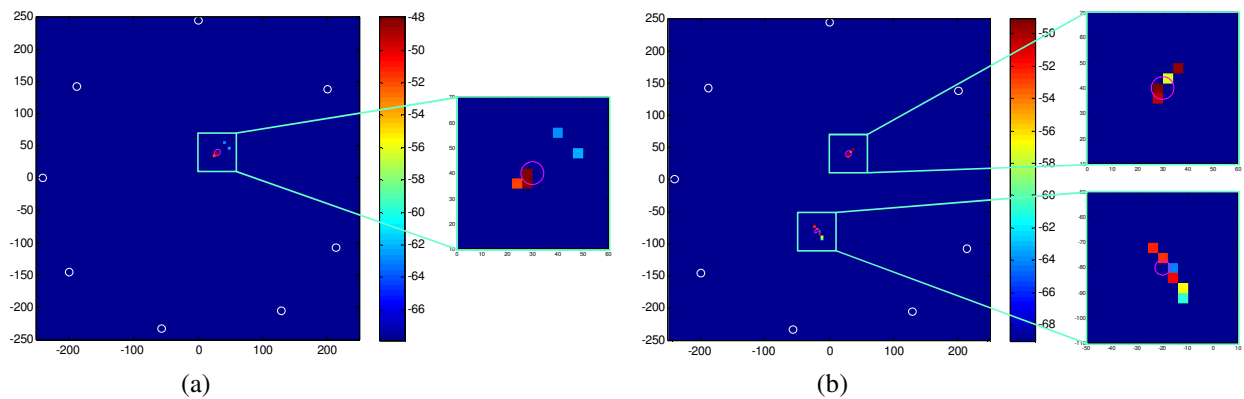

FIGURE 11. SR images from experimental data for glued-on masses. (a) Single scatterer and (b) two scatterers. Images are shown on a 20 dB color scale, and note zoomed views around scatterers. The white open circles are the transducer locations, and the red open circles are the locations of the scatterers.

Development of the SR method is significant because it is the first time that the sparsity assumption has been effectively incorporated into imaging of scatterers. Additional information can be found in [33].

The three methods just described – DAS, MVDR, and SR – all rely upon baseline subtraction to separate scattered signals from direct arrivals and geometrical reflections. However, baseline data may not be available for some structures, or the baseline data may have been recorded under mismatched environmental or operational conditions. For such a situation a baseline-free imaging method has been developed that is based upon estimating the source waveform and then adaptively removing the direct arrival from each received signal. This method is most effective when there are a large number of receivers, such as is the case when guided wave signals are recorded with a scanning laser vibrometer or a scanned air-coupled transducer. Figure 12 illustrates the experimental geometry when there is one source and the receivers are located on the periphery of the area of interest. This situation may arise when an *in situ* sparse array system indicates that damage may be present and confirmation is needed using embedded sources and a fast, external data acquisition method.
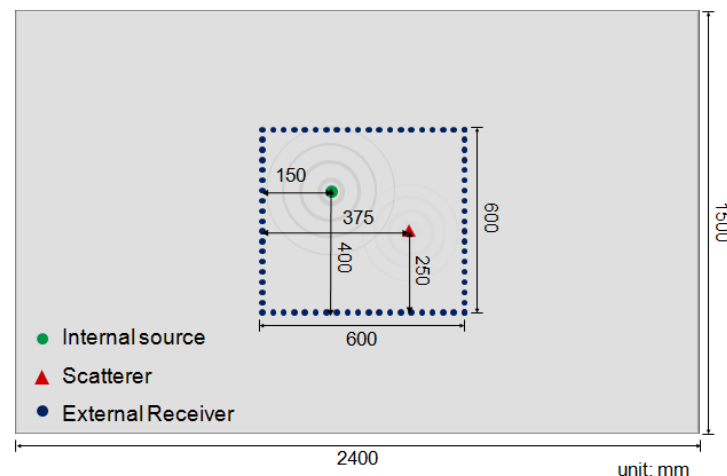

FIGURE 12. Diagram of a 2400 mm × 1500 mm × 3.18 mm 6061 aluminum plate with a centered region of interest that is 600 mm × 600 mm. Shown are the internal source, external receivers, and scatterer.

If DAS imaging is directly applied to the received signals, the source dominates and the resulting image shows only the source, as shown in Figure 13(a). After the source location and time function are estimated from the data and removed, the residual signals can be used to image the scatterer, as shown in Figure 13(b). The imaging artifacts shown in the lower right corner are caused by edge reflections that are not eliminated by adaptive source removal. Additional work using simulated data showed the feasibility of estimating and removing edge reflections since such reflections appear as "mirror" sources and can be located and estimated similarly to the direct (real) source. The significance of this work is that it illustrates the feasibility of imaging scatterers without using baseline data even when the scatterer is directly between the source and some of the receivers. Additional information can be found in [17,30,35].
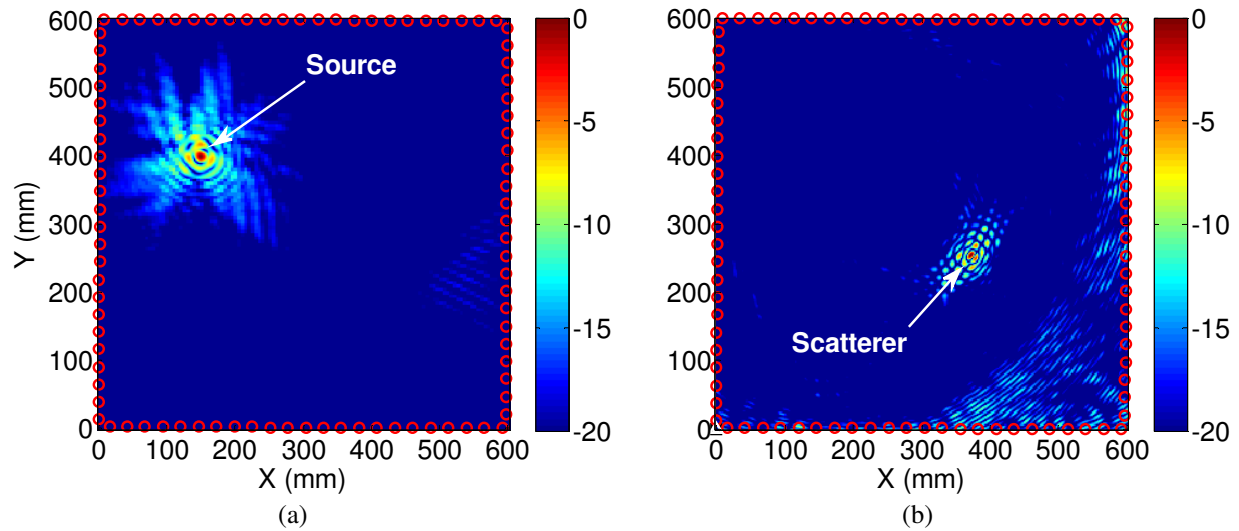
FIGURE 13. Images constructed from experimental data. (a) Delay-and-sum image of the source constructed from the raw data. (b) Delay-and-sum image of the scatterer constructed from signals with direct arrivals removed via adaptive source removal. Each image is shown on a 20 dB scale normalized by its maximum pixel value, and the circles around the periphery indicate the receiver locations.

3.2   Damage characterization via guided wave imaging

The MVDR method requires that the expected scattering pattern be known (or estimated) prior to imaging, which can be problematic. On the other hand, if several types of scatterers are possible and their scattering patterns are known, MVDR has the advantage of being able to not only locate the scatterers but to characterize them. This idea is illustrated using data recorded from two different notches cut in an aluminum plate. A 15 mm long notch oriented at +45° was located in the lower left corner of the plate, and a similar notch oriented at -45° was located near the center of the plate. These notches, like cracks, are highly directional scatterers, and thus the two notches at the two different orientations scatter the guided waves quite differently.

Figure 14(a) shows the image generated of the +45° notch using the correct scattering pattern, whereas Figure 14(b) is the corresponding image on the same scale but created using the scattering pattern of a notch at 90°. Clearly the response is almost 20 dB lower in amplitude when the incorrect scattering pattern is used for imaging. Figure 14(c) shows the maximum response for both notches as a function of the orientation angle of the assumed scattering pattern. The peak locations of each curve agree well with the actual notch orientations. These results indicate that small scatterers can be characterized using a sparse array if their scattering characteristics are known and are sufficiently different. This idea is much different than traditional methods for characterizing scatterers using many measurements to directly trace out the scattering pattern. Most importantly, it points the way to practical, in situ damage characterization using a very small number of transducers. Additional results can be found in [28].
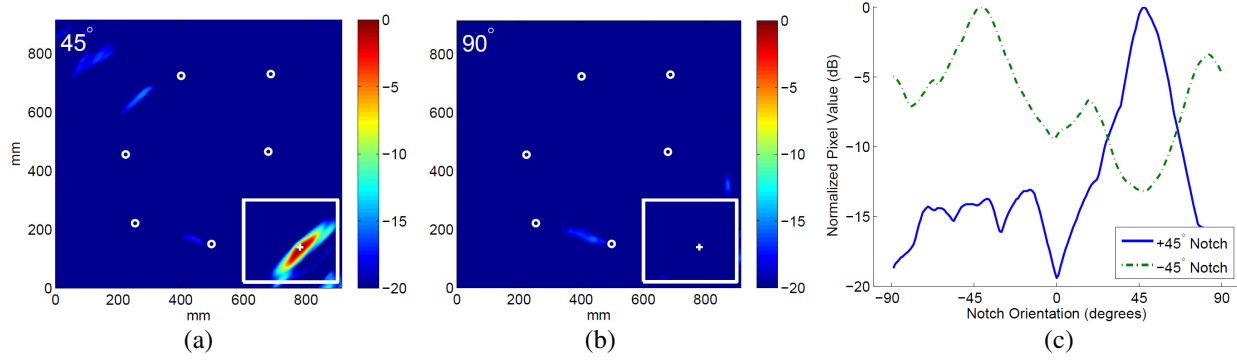
FIGURE 14. Example of damage characterization via MVDR imaging. (a) MVDR image of a +45° notch using the correct scattering pattern. (b) MVDR image of the same notch but using an incorrect scattering pattern. (c) Maximum MVDR image amplitudes for both notches assuming scattering patterns corresponding to notch orientations of -90° to +90°.

3.3   Model-based parameter estimation for dispersive wave propagation

Accurate knowledge of transducer locations, expected propagation loss, and dispersion curves is necessary for best performance of NDE and SHM methods employing guided waves. A model-based parameter estimate (MBPE) algorithm has been developed that simultaneously estimates these parameters along with transmitter and receiver transfer functions. The MBPE algorithm is scalable to accommodate two or more receivers and requires that direct arrivals for the mode of interest be isolated in time. Assuming a homogeneous, isotropic plate, a frequency domain model of a noise-free guided wave signal $S(\omega)$ is

$$S(\omega) = T(\omega) R(\omega) \left[\frac{d}{\delta}\right]^{-p(\omega)} e^{-ik(\omega)d} . \tag{2}$$

Here $T(\omega)$ is the transmitter transfer function, $R(\omega)$ is the receiver transfer function, d is the distance between transmitter and receiver, δ is a reference distance, $p(\omega)$ is the propagation loss, and $k(\omega)$ is the dispersion. The algorithm is able to estimate all parameters on the right hand side of the above equation with minimal a priori information, and can readily accommodate either common transducer transfer functions (same for all transducers), individual ones (different for each transducer), or various combinations (e.g., one transmitter, multiple receivers).

Figure 15 illustrates typical results for characterizing transducers and wave propagation between multiple transducers bonded to an aluminum plate. There were six transducers, which result in 15 unique transducer pairs. Received signals are shown in Figure 15(a) and (b) displayed as a waterfall plot where the vertical axis is the transducer separation distance. The estimated signals as calculated from the estimated parameters are also shown on the plots. Figures 15(a) and (b) indicate the improved model match achieved when each transducer is permitted to have individual transmitter and receiver transfer functions rather than assuming that they are all identical. Figure 15(c) shows how well estimated dispersion curves for the two cases match the nominal curve.

The MBPE algorithm is the first such method that has been able to simultaneously estimate dispersion curves, transfer functions, propagation loss and propagation distances, and is applicable to other wave propagation domains (e.g., acoustic and electromagnetic). Detailed algorithmic descriptions and additional results can be found in [15,16,26].
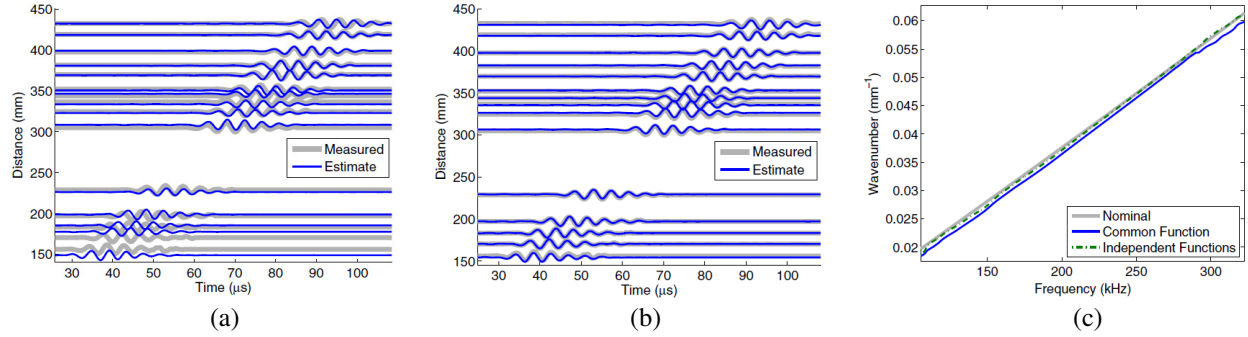

FIGURE 15. Model-based parameter estimation results for experimental data. (a) Experimental and estimated signals using common transducer transfer functions. (b) Experimental and estimated signals using individual transmitter and receiver transfer functions. (c) Comparison of estimated and nominal dispersion curves.

Although the MBPE algorithm is useful by itself for estimating dispersion, propagation loss, etc., its real strength is evident when it is combined with MVDR to achieve significantly improved imaging results. Recall the improvement in resolution achieved using phase information as was shown in Figure 10(c). For that experiment dispersion was minimal and it was possible to obtain reasonable images without using dispersion compensation. In contrast, Figure 16(a), which was obtained using a larger plate and a different mode/frequency combination, shows the MVDR image formed from raw signals with no dispersion compensation. Clearly the image is completely unusable. In contrast, Figure 16(b) illustrates the improvement obtained when incorporating dispersion compensation prior to imaging using nominal dispersion curves. Figure 7(c) shows the even more dramatic improvement achieved by using dispersive curves estimated from the MBPE algorithm. Refer to [32] for more details.
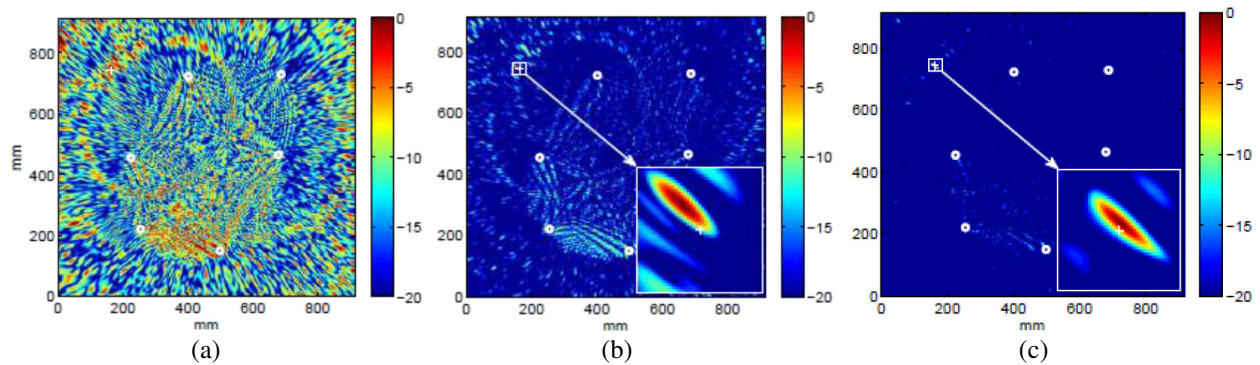

FIGURE 16. MVDR imaging using phase information. (a) No dispersion compensation, (b) compensation using nominal dispersion curves, and (c) compensation using dispersion curves estimated with the MBPE algorithm. All images are shown on a 20 dB scale normalized to the image peak value.

3.4   Environmental effects on guided wave propagation

Variable operational and environmental conditions can adversely affect the performance of SHM systems by causing changes in guided wave signals that may either be mistaken for damage or mask damage. The three most common such conditions are temperature, stresses, and surface wetting; temperature and surface wetting were considered as part of this project.

The basic idea for most, if not all, temperature compensation methods is to (1) record baseline signals at a range of temperatures, (2) find the baseline signal that best matches the current signal of interest, and (3) adjust this signal to better match the current signal. The first two steps are usually referred to as optimal baseline selection (OBS), and the last by baseline signal stretch (BSS) because signal stretching (with slight time shifts) is the usual method to achieve matching. This basic method was improved in several significant ways as summarized in Table 3:

TABLE 3. Summary of changes to the OBS+BSS temperature compensation method.

Original Method	New Method
1. Stretch implemented in the frequency domain	1. Stretch implemented in the time domain

2. Stretch/shift algorithm:
   a. Stretch computed from lags of short time cross correlation plotted at time window centers
   b. Shift determined by cross correlation of entire stretched waveforms
	2. Stretch/shift algorithm:
	   a. Stretch computed from lags of short time cross correlation plotted at center of energy
	   b. Shift is y-intercept of lags vs. time

3. Same baseline set selected for all pairs	3. Individual baseline selected for each pair
4. Single baseline used to construct matched signal	4. Weighted average of two baselines used to construct matched signal

These changes resulted in significant improvement in temperature compensation as measured by the detection margin – the dB difference in the residual signal before and after damage. Table 4 is a tabulation of improvement for five representative transducer pairs from a specific aluminum plate experiment. Note that the new method was able to achieve significantly better performance while using less data (smaller time window and lower sampling frequency). More details regarding temperature compensation results are found in [19,21,34].

TABLE 4.   Summary of detection margins for the original and new methods of temperature compensation.

Transducer Pair	Detection Margin (dB)		
	Original Method		New Method
	4000 μs, 25 MHz	1000 μs, 5 MHz	1000 μs, 5 MHz
1-3	4.30	1.30	7.06
2-3	3.10	2.48	6.83
3-4	4.80	1.82	6.16
3-5	1.02	-2.80	4.09
3-6	3.49	1.14	3.91

Surface wetting was also investigated as a part of this project. A representative structure was fabricated consisting of a stiffened aluminum plate, PZT disc-type transducers were bonded onto one surface, and surface wetting was introduced by applying random droplets of water onto the opposite surface. Frequencies from 100 to 400 kHz were studied by analyzing residual signals before and after application of varying amounts of surface wetting. Results, which are not shown here, indicate that even very small amounts of surface wetting may be mistaken for damage over the entire frequency range considered [31].

3.5   Supporting efforts

Additional research activities have taken place to support the primary objectives of in situ damage detection and characterization. These include (1) transducer diagnosis, (2) broadband chirp excitations, (3) evaluation of array performance, and (4) additional guided wave imaging studies. These efforts are briefly summarized as follows.

Transducer diagnosis is very important for SHM because of the danger that a faulty transducer may either mask damage or be mistaken for damage. An in situ transducer diagnosis method based upon signal reciprocity has been developed and implemented. It is well-known that if identical transducers are affixed to locations on a structure where the local geometry is identical (i.e., the plate thickness), signals are identical if transmitter and receiver are interchanged. However, if one of the transducers (or its bond) is damaged, then signal reciprocity will no longer hold. The transducer diagnosis method compares reciprocal signals for all transducers in a spatially distributed array, and uses appropriate statistics to determine which, if any, are faulty. At least two transducers in the array must remain undamaged to correctly identify all bad transducers. Details are available in references [18,20,25].

It is usually advantageous to generate relatively narrowband guided wave signals to achieve both mode purity and reasonable time resolution. Determining the optimal frequency and pulse width for the excitation signal is usually an iterative process that may be quite time-consuming. It may also be desired to acquire data at multiple frequencies to obtain additional information about possible damage. A signal processing method was evaluated and implemented to obtain all required broadband information in a single measurement via a chirp excitation. It was shown that recovered narrowband signals are virtually identical to those obtained by conventional tone burst excitations, but generally with reduced noise levels. This method of chirp excitation is also anticipated to enable practical implementation of a variety of guided wave systems and methods because of the significantly reduced time for data acquisition. Details of chirp-based methods are found in [27,36,49].

Of practical importance is development of a methodology for evaluating sparse array performance for a particular array configuration, structural component, and imaging method. The basic idea is to evaluate the damage detection capability at a specific spatial location by comparing the maximum amplitude achieved by the imaging algorithm at that location for two cases: (1) the damage is located at that location, and (2) the damage is located somewhere else. For the second case of the damage being located elsewhere, an indication at the specific location being considered would be an artifact. By simulating damage in every possible location on the structure, a figure of merit can be defined and quantified for the specific array geometry. This

methodology has enabled the performance of different array configurations and imaging algorithms to be quantified and compared for a particular structure, and results are reported in [28]. It is anticipated that this type of methodology will be used as part of the design process for critical SHM systems.

Additional studies on guided wave imaging have been performed as part of the project as described in reference [41]. Like the results shown in Figures 16(b) and (c), the imaging procedure operates on signals in which dispersion has been compensated. The dispersion compensation approach in [41] is based upon a transformation of the frequency scale that is designed to match a specific wave mode. The process results in compensated signals with compact time support, which make the development of imaging algorithms based on delay and sum or basis pursuit [47] procedures particularly convenient and effective.

4.   Structural Effects of Damage

Efforts have been devoted to the development of a modeling framework in support of experimental activities for the detection and quantification of damage in structural components. Efficient wave propagation models are extremely important for the simulation of the interaction of propagating waves with localized defects. Such models enable the development of novel damage detection algorithms and the study of their effectiveness through parametric studies. The application of Finite Element (FE) packages for the simulation of multi-dimensional wave propagation in structures is often time consuming, and can be affected by inaccuracies related to the quality of the mesh and the numerical integration parameters used for the analysis. It is therefore important that significant attention is devoted to simulation tools dedicated to guided wave propagation in damaged components. In our effort, spectral finite element models of one-dimensional waveguides are developed in conjunction with perturbation studies that allow the introduction of simplified models of damage. In addition, multi-scale FE formulations have been implemented for the analysis of guided wave propagation in damage plates. Simulation results are used for the numerical estimation of scattering coefficients, which can support the imaging algorithms developed as part of the project. Measurements of full wavefield data complement and validate the simulation results.

4.1   Complex one-dimensional waveguides

The first step in developing procedures capable of damage localization and quantification is understanding the effect of damage on waves propagating in structures. The current work gives a numerical model of a waveguide with a localized material or/and geometrical degradation (Figure 17). Particular cases of this type of damage include notches (or thickness reduction), delaminations, and local stiffness reduction. The beam's wave propagation response is simulated
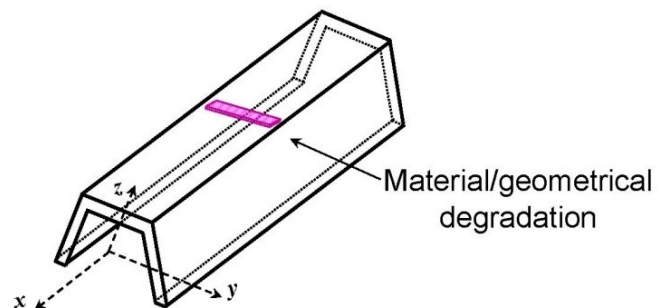

FIGURE 17. Beam geometry.

through the combined application of perturbation techniques and the Spectral Finite Element Method (SFEM). Damage is introduced as a small perturbation of mechanical or geometry properties so that perturbation techniques can be employed to describe the structure's dynamic behavior.

The resulting perturbation equations are solved in the frequency domain using the Spectral Finite Element Method (SFEM). SFEM, which is very similar to the Finite Element Method but formulated in the frequency domain, gives very accurate solutions for the dynamic analysis of structures because it is based on the exact dynamic stiffness matrix by using the exact shape functions. The resulting numerical tool allows efficient computation of the wave propagation response and the analysis of the effects of localized damage of various extent and location. The dynamic behavior of damaged beams is described through a general higher order model which couples different Lamb and/or shear horizontal modes, thus allowing the prediction of mode conversion phenomena.

Figure 18 plots dispersion curves for an aluminum beam and compares them to analytical results. The frequency range is large enough such that higher modes are included; only a few selected modes are shown. For a second example, the same beam was used, but the frequency interval was restricted to include only the first symmetric S_0 and asymmetric A_0 Lamb modes. An in-plane longitudinal load whose variation in time is described by a Hanning modulated sine burst at 100 kHz is applied on the top of the plate. Figure 19 presents the variation of the in-plane and out-of-plane displacements in time and space, on a common scale. As expected, the amplitude of S_0 is larger in-plane whereas the amplitude of A_0 is larger out-of-plane. Based on these results, the computed velocities compare well with the analytical ones for both S_0 and A_0.
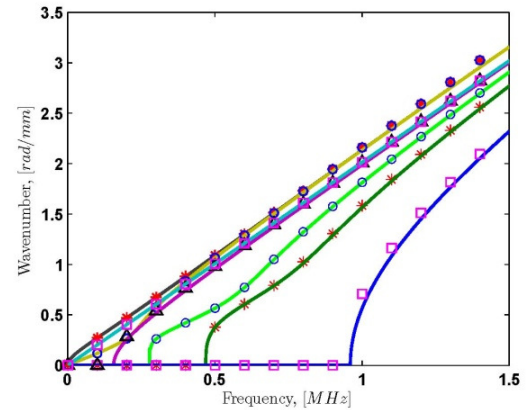

FIGURE 18. Dispersion curves showing selected modes. Solid lines−SFEM; symbols−analytical results;
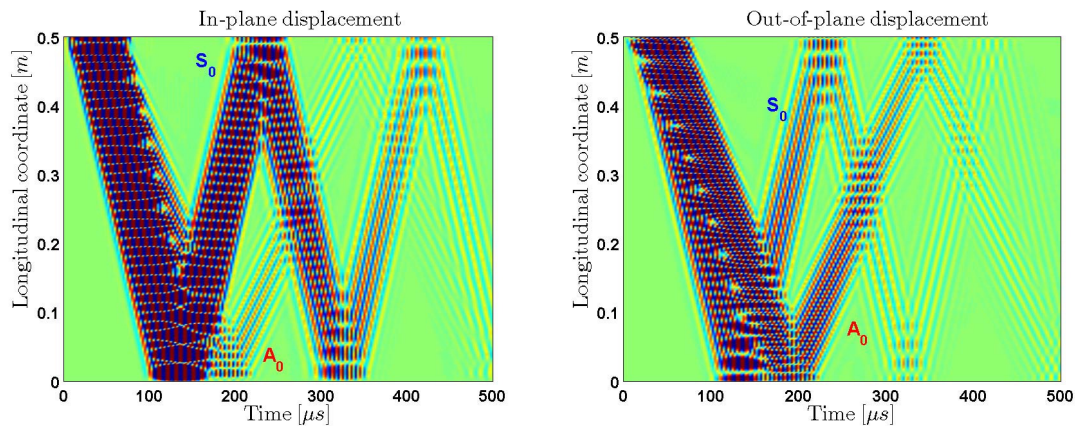

FIGURE 19. Displacements as function of time and longitudinal coordinate showing both S_0 and A_0 Lamb modes: In-plane displacement (left); Out-of-plane displacement (right).

The results from the simulations on damaged 1D waveguides have been exploited to formulate a damage-localization process based on the evaluation of the phase of the response recorded at a large number of points along the length of the waveguide. Estimation of the gradient of the phase effectively highlights the presence of damage as a secondary wave source, which is described in detail in [42]. In addition, multi-component wave propagation and mode conversion due to damage is studied through the developed approach, and subsequently validated through the multicomponent measurement procedure presented in [43,45].

4.2   Experimental validation

In conjunction with the numerical studies, simple experimental validations for the work were carried out. In particular, wave propagation data were recorded using a scanning laser vibrometer to obtain a detailed mapping of the propagation characteristics of guided waves along a complex waveguide. Detailed experiments of this kind for validation of wave propagation code have never before been performed, and therefore have advanced the state-of-the-art both in regards to the estimation of the accuracy of the numerical code, and with respect to the understanding of the characteristics of guided waves along the waveguide.

The experiments were performed on an angle beam (see Figure 20) that was excited by a piezoelectric disc mounted on the top flange. The cross section consisted of two perpendicular flanges, each of which was monitored during two separate scans performed at different times. The excitation was reproduced repeatably through the two scans, so that the separate acquisitions could be "stitched" in a postprocessing phase upon completion of the measurements. Figures 20(b) and 20(c) show snapshots of the resulting scans obtained at different propagation times. These results clearly show the propagation characteristics for the specific angle beam and allow their comparison with the numerical predictions and therefore the validation of the codes.
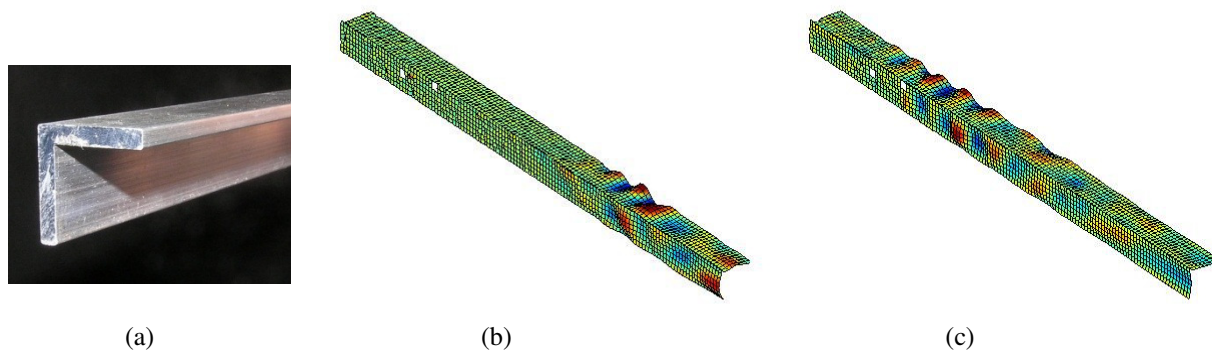

(a)   (b)   (c)

FIGURE 20. (a) Angle beam used for experimental validation. (b,c) Snapshots of measured propagating wave.

4.3   Extension to damaged plate structures

Wave propagation in a damaged rectangular plate can similarly be considered using a perturbation approach where a local thickness variation describes the spatial extension and the severity of the damaged area. A set of results for a sine burst excitation and the interaction of the propagation of a wave with a longitudinal slit are shown in Figure 21.
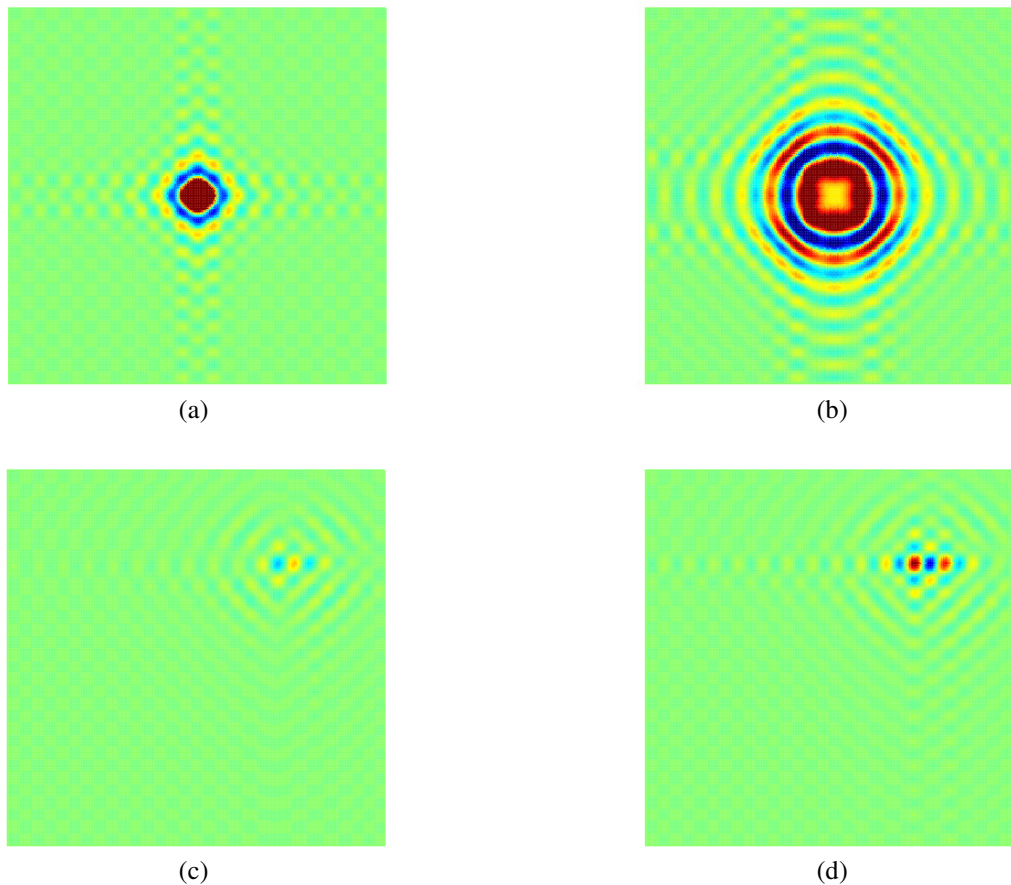
FIGURE 21. (a,b) Snapshots of the transverse displacement history of a plate with built-in damage forced by imposing an initial displacement at the center. (c,d) Development of the perturbed solution.

4.4   Wavefield imaging for baseline-free characterization of scatterers

Full acoustic wavefield data were acquired from an aluminum plate with various structural discontinuities and artificial defects using an air-coupled transducer mounted on a scanning stage. Piezoelectric transducers permanently mounted on the specimen were used as wave sources. These source transducers were elements of a permanently attached sparse array. As shown in Figure 22, wavefield images clearly show details of guided waves as they propagate outward from the source, reflect from specimen boundaries, and scatter from discontinuities within the structure.   Distinct S_0 and A_0 Lamb incident waves are directly visible on these constant time snapshots of the captured wavefield. However, as can be seen in the figure, the waves propagating outward from the source and reflected from boundaries obscure the weaker waves that are scattered from defects.

To facilitate analysis of the weaker scattered waves, source waves are removed from the wavefield data using both time and frequency domain methods. Figure 23(a) shows a snapshot of a zoomed wavefield image that includes the incident wave and the wave scattered from a hole. Figure 23(b) shows the same image after the incident wave has been partially removed using an

adaptive time domain subtraction method. Figure 23(c) shows the same image after the forward propagating wave has been removed by filtering in the $\omega - k_r$ domain. Both of these methods are effective at removing the incident wave, but they also remove portions of the scattered wave.
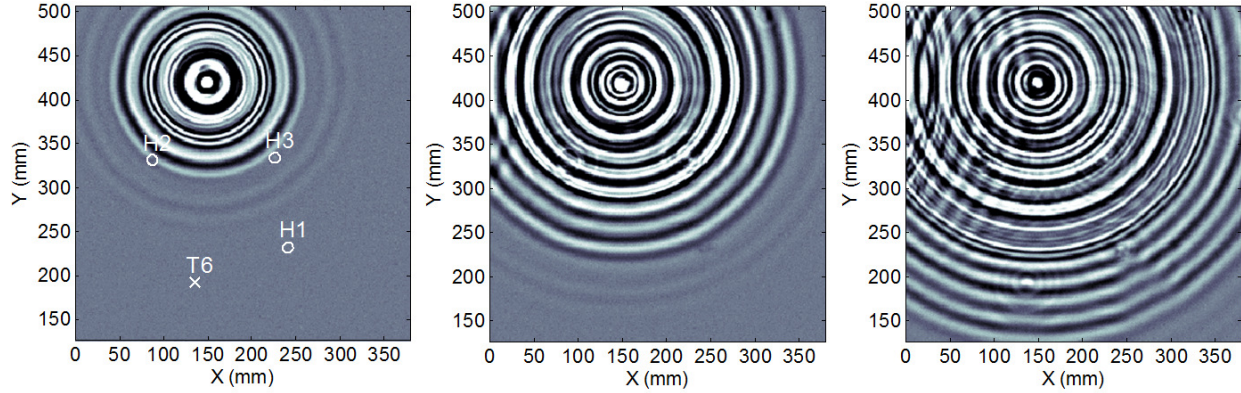

FIGURE 22. Acoustic wavefield images at propagation times of 30, 50 and 70 μs for transmitting on the transducer at (X=150 mm, Y=420 mm). Hole and transducer locations are shown on the 30 μs images, and scattering from these locations is observable on the later time images.
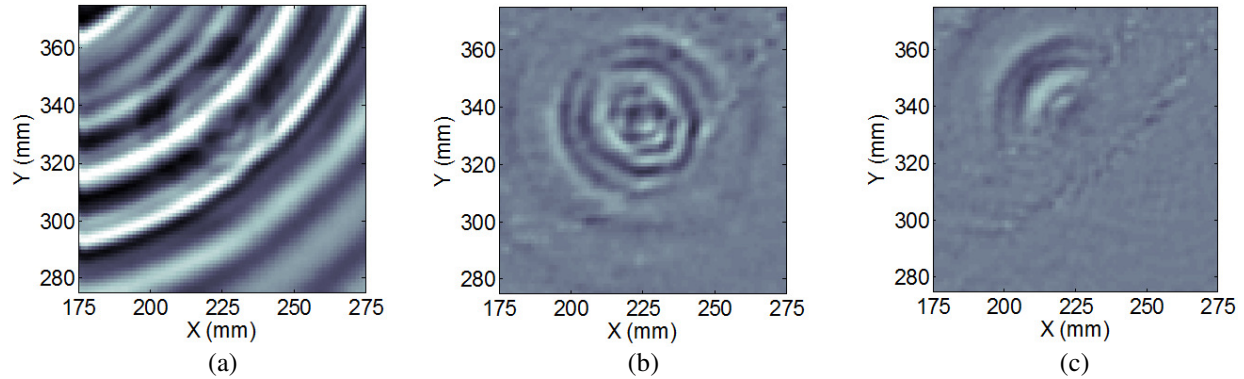

FIGURE 23. Analysis of waveforms from scan in a zoomed region around Hole H3. Waveform data were spatially windowed over the zoomed region, windowed in time from 0 to 50.6 μs, and windowed in the frequency domain from 0.2 MHz to 0.3 MHz. (a) Snapshot of the originally wavefield in a zoomed region encompassing the hole. (b) Snapshot of the wavefield using the time domain source removal method as applied to the original wavefields. (c) Snapshot of the wavefield after removing outward going waves in the $\omega - k_r$ domain (as applied to the original wavefield).

Results from the two methods are fused to obtain more complete information about the scattered wavefields. Figure 24 shows polar representations of successive scattered fields, first from a through hole, then the hole with a corner notch, and finally the hole with a through notch; the motivation is to simulate a growing crack. Plots are shown for source waves incident on the notch from two directions, one toward the side of the notch (transducer T1, top row) and the other toward the end of the notch (transducer T2, bottom row). The directional characteristics of the scatterer with respect to the source wave direction are evident along with the varying degrees

of mode conversion as the symmetry changes. These polar plots of the wavefields scattered from two incident wave orientations illustrate one method for experimentally obtaining quantitative flaw scattering characteristics without using damage-free baseline data.
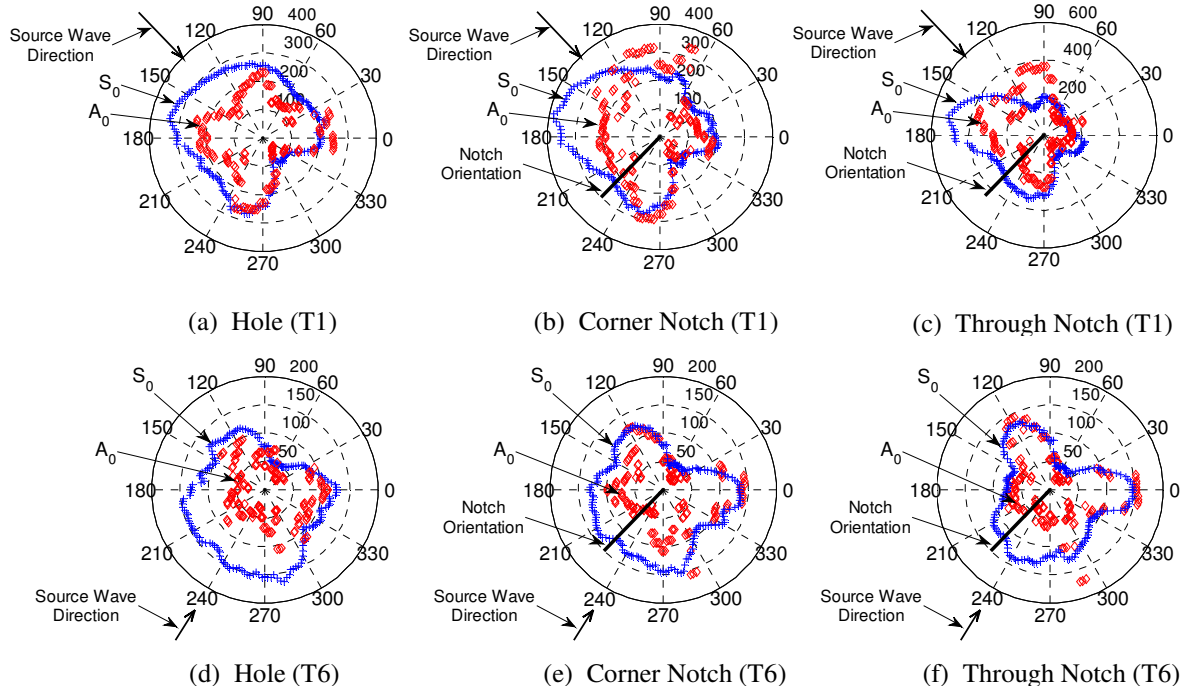

FIGURE 24. Scattered wavefields calculated for hole H3 by combining results from time domain method and the $\omega - k_r$ domain method to remove the incident wave. (a,b,c) Polar plots of S_0 and A_0 wave mode amplitudes for an incident wave direction of about 135° (approximately broadside to the notch). (d,e,f) Polar plots of S_0 and A_0 wave mode amplitudes for an incident wave direction of about 240° (approximately end-on to the notch).

Details of the frequency/wavenumber filtering procedure for incident wave removal and mode separation, along with other wavefield methods, can be found in [37-39,48-50]. Further development of the method, using "curvelets" for the decomposition of the wavefield data in its modal constituents, is presented in [44].

4.5   Application of the multi-scale finite element method to wave propagation problems in damaged structures

The effort explored the possibility to extend the field of application of the Multi-Scale Finite Element Method (MsFEM) to structural mechanics problems that involve localized geometrical discontinuities like cracks or notches. The main idea is to construct FEs with an arbitrary number of edge nodes that describe the actual geometry of the damage with shape functions that are defined as local solutions of the differential operator of the specific problem. The efficiency of the method is demonstrated through selected numerical examples that constitute classical problems of great interest to the structural health monitoring community. Details of the method can be found in [46]. The MsFEM is a development from a similar approach, operating in the

frequency domain, previously documented in [40]. The need for a new formulation was motivated by the considerable computational cost associated with the formulation of proper interface conditions with boundary mesh, and the computation of the interaction forces in the frequency domain. The current MsFEM has proven to be a significant development in terms of reduction of computation costs and convenience of implementation.

4.5.1   Background

The proposed multiscale FE scheme introduces generalized finite elements with arbitrary shape and arbitrary number of nodes along the boundaries or within the element itself. As illustrated in Figure 25, multiscale elements (MsE) can be used to naturally model inclusions or damage since the associated degrees of freedom are assembled as part of the global FE system of equations. The proposed method defines multiscale shape functions as the displacement field generated by imposing a unit displacement at a specific node while all other element freedoms are fixed. As shown in Figure 25(c), shape functions are implemented numerically by solving a fine-scale FE problem within the MsE itself using an auxiliary fine-scale triangular mesh.
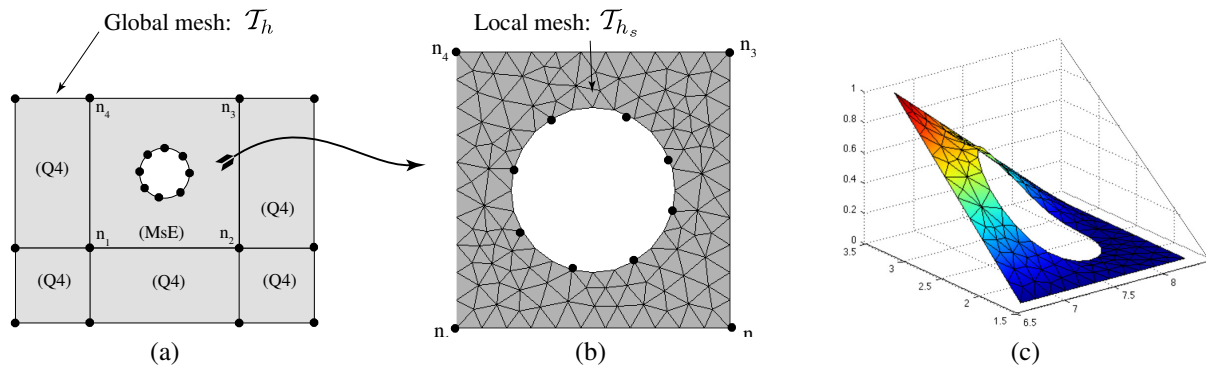

FIGURE 25. Schematic of the Multiscale finite element method: (a) configuration of a multiscale finite element (MsE) surrounded by a mesh of bilinear quad elements (Q4), (b) detail of fine-scale mesh within the MsE, and (c) example of a multiscale shape function.

4.5.2   Model validation analysis

A direct comparison between the wavefield computed with MsFEM and standard FEM is shown in Figure 26, which shows side-by-side results of the two approaches at different simulation instants. With both strategies, the global discretizations correctly capture the propagation of elastic waves on the large scales. When only standard finite elements are used, the need to correctly model the small inclusion requires uniformly refining the computational grid with severe consequences on the global computational efficiency. The CPU time required by the MsFEM to integrate the dynamic equation of motion is found to be more than 90% smaller when compared with the FEM simulations.
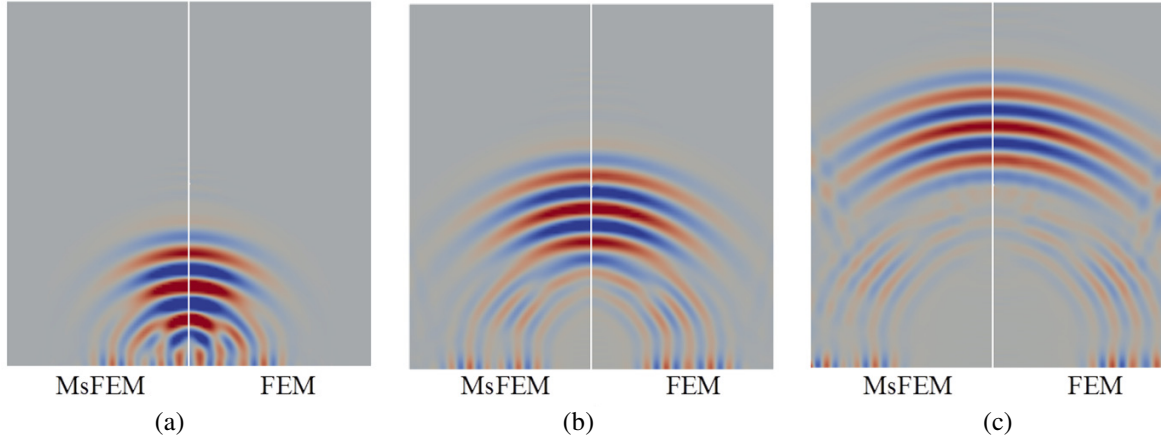
FIGURE 26. Comparison between the displacement field computed with the proposed MsFEM and the standard FEM at three different time steps: (a) $t_1 = 4.0$ ms, (b) $t_2 = 6.0$ ms, and (c) $t_3 = 8.0$ ms.

4.5.3   Application to scattering analysis

The proposed MsFEM was applied to the scattering problem of incident plane waves from defects of different size and shape. The computational domain consisted of a square elastic region ($Lx = Ly = 120$ mm) made of aluminum where plane stress conditions are assumed. An elliptic imperfection, with axis Ra and Rb=Ra/2, was located at the geometric center of the considered domain, and numerical simulations were conducted for a series of configurations limited to significant variations of the damage parameters. In order to validate the model and scattering algorithm, results are compared with available analytical solutions as shown in Figure 27.
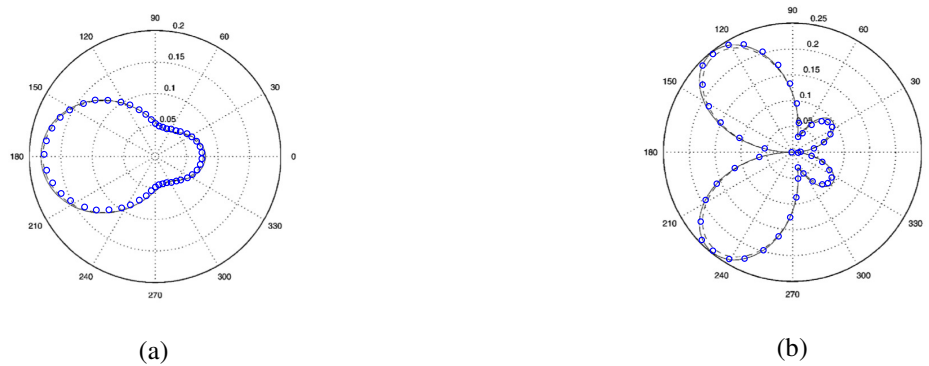

FIGURE 27. Scattering directivity plots for the dominating in-plane displacement components of the propagating modes: (a) scattered S0 wave, and (b) scattered SH0 wave. Analytical (solid line), MsFEM (o-markers).

The directivity patterns of several damage configurations were calculated with the propsed MsFEM. Figure 28 shows a series of results obtained for an elliptic defect with the major axis of length Ra perpendicular to the incident wave direction. All plots confirm that the S0 wave is scattered mainly forward and backward (i.e., at 0° and 180°), while the SH0 wave is scattered mainly in the transverse direction. It can be also noted that for all types of inclusions the

magnitude of the scattered field decreases several orders of magnitude as the diameter of the damage reduces, while the overall directionality pattern remains qualitatively the same. It is finally worth mentioning that all the present scattering data are computed with the same numerical grid, slightly adjusted only in the central region to accommodate different inclusions but all requiring the same computational time.
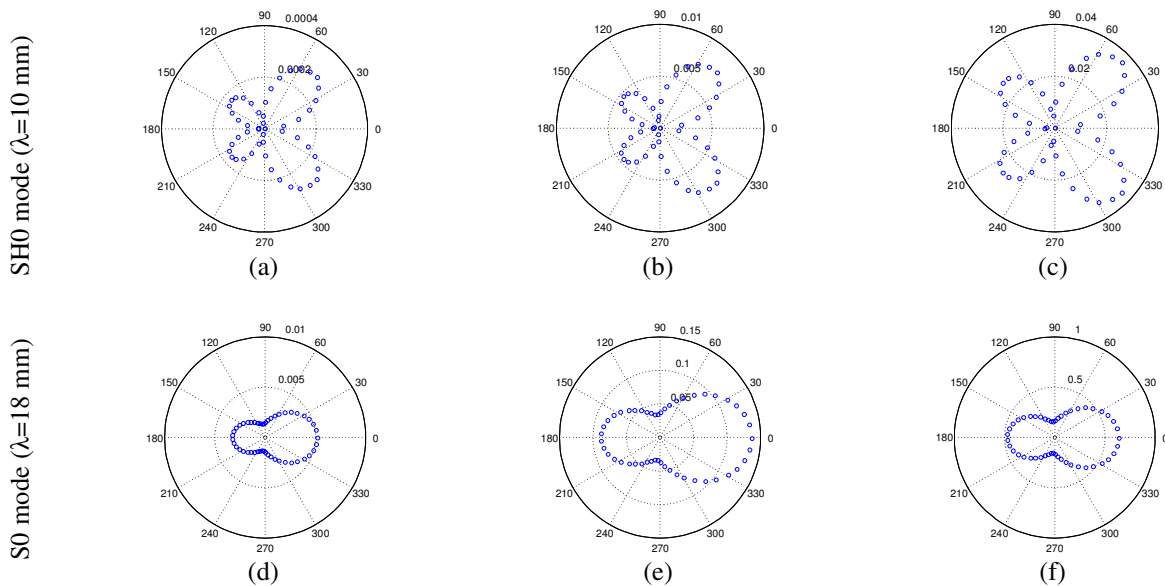

FIGURE 28. Scattering plots from elliptic defects for an incoming wave at 0 degrees (incident from the left). (a),(d) Ra=0.1mm. (b),(e) Ra=0.5mm. (c),(f) Ra=1.0 mm.

5. References

The following list of references includes all publications to date resulting from this project. Comprehensive literature reviews may be found in these references.

<u>Nonlinear Ultrasonics</u>

1. C. Pruell, J.-Y. Kim, J. Qu and L. J. Jacobs, "Evaluation of fatigue damage using nonlinear guided waves," *Smart Materials and Structures,* **18**, 035003 (7 pages), 2009.

2. C. Pruell, J.-Y. Kim, J. Qu and L. J. Jacobs, "Evaluation of fatigue damage using nonlinear guided waves," *Review of Progress in Quantitative Nondestructive Evaluation*, D. O. Thompson and D. E. Chimenti (Eds.), American Institute of Physics, **28A**, pp. 201-208, 2009.

3. C. Pruell, J.-Y. Kim, J. Qu and L. J. Jacobs, "A nonlinear guided wave technique for evaluating plasticity-driven material damage in a metal plate," *NDT&E International,* **42**, pp. 199-203, 2009.

4. Braun, M., Jacobs, L.J., Qu, J. and Kuechler, S., "Determination of third-order elastic constants using second-harmonic generation in an elastic material with quadratic nonlinearity," *Review of Progress in Quantitative Nondestructive Evaluation*, D. O. Thompson and D. E. Chimenti (Eds.), American Institute of Physics, **28A**, pp. 246-253, 2009.

5. M. F. Mueller, J.-Y. Kim, J. Qu, and L. J. Jacobs, "Characteristics of second harmonic generation of Lamb waves in nonlinear elastic plates," *Journal of the Acoustical Society of America,* **127** (4), pp. 2141-2152, 2010.

6. M. Mueller, J.-Y. Kim, J. Qu, and L. J. Jacobs, "On the excitability of second harmonic Lamb waves in isotropic plates," *Review of Progress in Quantitative Nondestructive Evaluation*, D. O. Thompson and D. E. Chimenti (Eds.), American Institute of Physics, **29A**, pp. 319-326, 2010.

7. Liu, M., Kim, J.-Y., Qu, J. and Jacobs, L.J., "Measuring residual stress using nonlinear ultrasound," *Review of Progress in Quantitative Nondestructive Evaluation*, D. O. Thompson and D. E. Chimenti (Eds.), American Institute of Physics, **29B**, pp. 1365-1372, 2010.

8. M. Liu, J.-Y. Kim, L. J. Jacobs, and J. Qu, "Experimental study of nonlinear Rayleigh wave propagation in shot-peened aluminum plates – feasibility of measuring residual stress," *NDT&E International,* **44**, pp. 67-74, 2011.

9. K. H. Matlack, J.-Y. Kim, J. Qu, and L. J. Jacobs, "On the efficient excitation of second harmonic generation using Lamb wave modes*," Review of Progress in Quantitative Nondestructive Evaluation*, D. O. Thompson and D. E. Chimenti (Eds.), American Institute of Physics, **30A**, pp. 291-297, 2011.

10. K. H. Matlack, J.-Y. Kim, L. J. Jacobs, and J. Qu, "Experimental characterization of efficient second harmonic generation of Lamb wave modes in a nonlinear elastic isotropic plate," *Journal of Applied Physics*, **109**, 014905, 2011.

11. K. H. Matlack, J.-Y. Kim, L. J. Jacobs, and J. Qu, "Feasibility of using nonlinear guided waves to measure acoustic nonlinearity of aluminum," *Proceedings of SPIE*, T. Kundu (Ed.), SPIE, **7984**, pp. 79840L:1-8, 2011.

12. J. Qu, L. J. Jacobs, and P. B. Nagy, "On the acoustic-radiation-induced strain and stress in elastic solids with quadratic nonlinearity," *Journal of the Acoustical Society of America*, **129**(6), pp. 3449-3452, 2011.

13. J. Qu, P. B. Nagy, and L. J. Jacobs, "Pulse propagation in an elastic medium with quadratic nonlinearity," *Journal of the Acoustical Society of America*, to appear 2012.

Spatially Distributed Arrays

14. J. E. Michaels, J. S. Hall and T. E. Michaels, "Adaptive imaging of damage from changes in guided wave signals recorded from spatially distributed arrays," *Proceedings of SPIE*, T. Kundu (Ed.), SPIE, **7295**, pp. 729515:1-11, 2009.

15. J. S. Hall and J. E. Michaels, "A model-based approach to dispersion and parameter estimation for ultrasonic guided waves," *Journal of the Acoustical Society of America*, **127**(2), pp. 920-930, 2010.

16. J. S. Hall and J. E. Michaels, "Model-based *in situ* parameter estimation of ultrasonic guided waves in an isotropic plate," *Review of Progress in Quantitative Nondestructive Evaluation*, D. O. Thompson and D. E. Chimenti (Eds.), American Institute of Physics, **29A**, pp. 137-144, 2010.

17. N. Gandhi, S. J. Lee, B. Xu, J. S. Hall, J. E. Michaels, T. E. Michaels and M. Ruzzene, "Beamforming of wavefield data from embedded sources for rapid follow-up inspection of inaccessible areas," *Review of Progress in Quantitative Nondestructive Evaluation*, D. O. Thompson and D. E. Chimenti (Eds.), American Institute of Physics, **29A**, pp. 184-191, 2010.

18. S. J. Lee, H. Sohn, J. E. Michaels and T. E. Michaels, "*In situ* detection of surface-mounted PZT transducer defects using linear reciprocity," *Review of Progress in Quantitative Nondestructive Evaluation*, D. O. Thompson and D. E. Chimenti (Eds.), American Institute of Physics, **29B**, pp. 1844-1851, 2010.

19. Z. Lu, S. J. Lee, J. E. Michaels and T. E. Michaels, "On the optimization of temperature compensation for guided wave structural health monitoring," *Review of Progress in Quantitative Nondestructive Evaluation*, D. O. Thompson and D. E. Chimenti (Eds.), American Institute of Physics, **29B**, pp. 1860-1867, 2010.

20. S. J. Lee, J. E. Michaels, T. E. Michaels and H. Sohn, "*In situ* PZT diagnostics using linear reciprocity under environmental and structural variations," *Proceedings of SPIE*, T. Kundu (Ed.), SPIE, **7650**, pp. 76500N:1-10, 2010.

21. A. J. Croxford, J. Moll, P. D. Wilcox and J. E. Michaels, "Efficient temperature compensation strategies for guided wave structural health monitoring," *Ultrasonics*, **50**, pp. 517-528, 2010.

22. J. S. Hall and J. E. Michaels, "Minimum variance ultrasonic imaging applied to an *in situ* sparse guided wave array," *IEEE Transactions on Ultrasonics, Ferroelectrics, and Frequency Control*, **57**(10), pp. 2311-2323, 2010.

23. J. S. Hall and J. E. Michaels, "Computational efficiency of ultrasonic guided wave imaging," *IEEE Transactions on Ultrasonics, Ferroelectrics, and Frequency Control*, **58**(1), pp. 244-248, 2011.

24. J. S. Hall, P. McKeon, L. Satyanarayan, J. E. Michaels, N. F. Declercq and Y. H. Berthelot, "Minimum variance guided wave imaging in a quasi-isotropic composite plate," *Smart Materials and Structures*, **20**, 025013 (8pp), 2011.

25. S. J. Lee, J. E. Michaels, H. Sohn and T. E. Michaels, "Guided wave-based PZT diagnostics via linear reciprocity," *AIAA Journal*, **49**(3), pp. 621-629, 2011.

26. J. S. Hall and J. E. Michaels, "Model-based parameter estimation for characterizing wave propagation in a homogeneous medium," *Inverse Problems*, **27**, 035002 (27pp), 2011.

27. J. E. Michaels, S. J. Lee, J. S. Hall and T. E. Michaels, "Multi-mode and multi-frequency guided wave imaging via chirp excitations," *Proceedings of SPIE*, T. Kundu (Ed.), SPIE, **7984**, pp. 79840I:1-11, 2011.

28. J. S. Hall, P. Fromme and J. E. Michaels, "Ultrasonic guided wave imaging for damage characterization," *2011 Aircraft Airworthiness & Sustainment Conference*, San Diego, CA, April 18-21, 2011 (available online at http://www.airworthiness.com).

29. J. S. Hall and J. E. Michaels, "Analysis of distributed sparse array configurations for guided wave imaging applications," *Review of Progress in Quantitative Nondestructive Evaluation*, D. O. Thompson and D. E. Chimenti (Eds.), American Institute of Physics, **30A**, pp. 859-866, 2011.

30. R. Levine, J. E. Michaels and S. J. Lee, "Boundary reflection compensation in guided wave baseline-free imaging," *Review of Progress in Quantitative Nondestructive Evaluation*, D. O. Thompson and D. E. Chimenti (Eds.), American Institute of Physics, **30A**,pp. 113-120, 2011.

31. H. Li, J. E. Michaels, S. J. Lee and T. E. Michaels, "Quantification of surface wetting in plate-like structures via guided waves," *Review of Progress in Quantitative Nondestructive Evaluation*, **31**, D. O. Thompson and D. E. Chimenti (Eds.), American Institute of Physics, to appear 2012.

32. J. S. Hall and J. E. Michaels, "Adaptive dispersion compensation for guided wave imaging," *Review of Progress in Quantitative Nondestructive Evaluation*, D. O. Thompson and D. E. Chimenti (Eds.), American Institute of Physics, **31**, to appear 2012.

33. R. M. Levine, J. E. Michaels and T. E. Michaels, "Guided wave localization of damage via sparse reconstruction," *Review of Progress in Quantitative Nondestructive Evaluation*, D. O. Thompson and D. E. Chimenti (Eds.), American Institute of Physics, **31**, to appear 2012.

34. J. E. Michaels, R.-J. Liou, J. P. Zutty and T. E. Michaels, "On the interpolation of ultrasonic guided wave signals," *Review of Progress in Quantitative Nondestructive Evaluation*, D. O. Thompson and D. E. Chimenti (Eds.), American Institute of Physics, **31**, to appear 2012.

35. S. J. Lee, N. Gandhi, J. S. Hall, J. E. Michaels, B. Xu, T. E. Michaels, and M. Ruzzene, "Baseline-free guided wave imaging via adaptive source removal," *Structural Health Monitoring*, to appear 2012.

36. J. E. Michaels, S. J. Lee, A. J. Croxford and P. D. Wilcox, "Chirp excitation of ultrasonic guided waves," Submitted to *Ultrasonics*, November 10, 2011.

Structural Effects of Damage

37. T. E. Michaels, M. Ruzzene and J. E. Michaels, "Frequency-wavenumber domain methods for analysis of incident and scattered guided waves," *Proceedings of SPIE*, T. Kundu (Ed.), SPIE, **7295**, pp. 729513:1-12, 2009.

38. T. E. Michaels, M. Ruzzene and J. E. Michaels, "Incident wave removal through frequency-wavenumber filtering of full wavefield data," *Review of Progress in Quantitative Nondestructive Evaluation*, D. O. Thompson and D. E. Chimenti (Eds.), American Institute of Physics, **28A**, pp. 604-611, 2009.

39. M. Ruzzene, B. Xu, S. J. Lee, T. E. Michaels and J. E. Michaels, "Damage visualization via beamforming of frequency-wavenumber filtered wavefield data," *Proceedings of SPIE*, T. Kundu (Ed.), SPIE, **7650**, pp. 76500L:1-8, 2010.

40. F. Casadei, and M. Ruzzene " Frequency-domain bridging multiscale method for wave propagation simulations in damaged structures" *Proceedings of SPIE*, T. Kundu (Ed.), SPIE, **7650**, pp. 76500N:1-10, 2010.

41. L. De Marchi, M. Ruzzene, B. Xu, E. Baravelli, A. Marzani, N. Speciale, "Warped frequency transform for damage detection using lamb waves", *Proceedings of SPIE*, T. Kundu (Ed.), SPIE, **7650**, pp. 76500N:1-10, 2010.

42. J. Ayers, N. Apetre, M. Ruzzene, and V. K. Sharma, "Phase gradient and mode conversion estimation in 1D damaged structures", *Structural Health Monitoring*, **10**(1), pp. 65-82, 2011.

43. J. T. Ayers, N. Apetre, M. Ruzzene and K. Sabra, "Measurement of Lamb wave polarization using a one-dimensional scanning laser vibrometer," *Journal of the Acoustical Society of America*, **129**(2), pp. 585-588, 2011.

44. L. De Marchi, E. Baravelli, M. Ruzzene and N. Speciale, "Guided waves filtering with warped curvelets", *Proceedings of SPIE*, T. Kundu (Ed.), SPIE, **7984**, pp. 79841Z:1-10, 2011.

45. J. T. Ayers, N. Apetre and M. Ruzzene, "Multiple component mode conversion coefficients via Lamb wave polarization measurements," *Proceedings of SPIE*, T. Kundu (Ed.), SPIE, **7984**, pp. 798411:1-17, 2011.

46. F. Casadei and M. Ruzzene, "Application of the multi-scale finite element method to wave propagation problems in damaged structures," *Proceedings of SPIE*, T. Kundu (Ed.), SPIE, **7984**, pp. 79842Q:1-12, 2011.

47. E. Baravelli, L. De Marchi, M. Ruzzene and N. Speciale, "High resolution damage imaging in flat and bent plate-like structures through warped-basis pursuit," *Proceedings of SPIE*, T. Kundu (Ed.), SPIE, **7984**, pp. 798412:1-11, 2011.

48. T. E. Michaels, J. E. Michaels and M. Ruzzene, "Frequency-wavenumber domain analysis of guided wavefields," *Ultrasonics*, **51**, pp. 452-466, 2011.

49. T. E. Michaels, J. E. Michaels, S. J. Lee and X. Chen, "Chirp generated acoustic wavefield images," *Proceedings of SPIE*, T. Kundu (Ed.), SPIE, **7984**, pp. 79840J:1-11, 2011.

50. T. E. Michaels, J. E. Michaels and M. Ruzzene, "Detection and sizing of subsurface impedance discontinuities using acoustic wavefield images," *Proceedings of the 8ᵗʰ International Workshop on Structural Health Monitoring*, F.-K. Chang (Ed.), DEStech Publications, Inc., Lancaster, PA, pp. 2215-2222, 2011.